Flow Boiling Heat Transfer on Micro Pin Fins Entrenched in a Microchannel

Santosh Krishnamurthy

Yoav Peles

Department of Mechanical, Aerospace, and
Nuclear Engineering,
Rensselaer Polytechnic Institute,
Troy, NY 12180

Flow boiling of 1-methoxyheptafluoropropane (HFE 7000) in 222 μm hydraulic diameter channels containing a single row of 24 inline 100 μm pin fins was studied for mass fluxes from 350 kg/m² s to 827 kg/m² s and wall heat fluxes from 10 W/cm² to 110 W/cm². Flow visualization revealed the existence of isolated bubbles, bubbles interacting, multiple flow, and annular flow. The observed flow patterns were mapped as a function of the boiling number and the normalized axial distance. The local heat transfer coefficient during subcooled boiling was measured and found to be considerably higher than the corresponding single-phase flow. Furthermore, a thermal performance evaluation comparison with a plain microchannel revealed that the presence of pin fins considerably enhanced the heat transfer coefficient. [DOI: 10.1115/1.4000878]

Keywords: micro pin fins, heat transfer coefficient, flow maps

1 Introduction

The level of device integration and the clock speed of microelectronic devices have been steadily increasing over the last several decades. This has resulted in a continuous increase in the power density of electronic devices, giving rise to the need for aggressive and effective cooling solutions. The recent development in microfabrication technology has enabled a new class of heat sinks for high heat flux applications made of microelectromechanical system (MEMS) based microchannel. Microchannels with micro pin fins have been receiving attention because they can significantly enhance the performance of heat sinks compared with plain microchannels. As a result, a research on flow boiling and single-phase flow in micro-pin fin heat sinks has been carried out by several groups [1–12]. It is well known that heat transfer during subcooled flow boiling can be significantly enhanced compared with single-phase liquid flow. However, very limited studies have been performed to elucidate the heat transfer characteristics of subcooled boiling in micro pin fin configurations.

In conventional scale, subcooled flow boiling has been extensively studied for in-tube systems and various models have been developed to predict the heat transfer rates. These methods can be broadly classified into three categories, namely: empirical correlations to predict the wall heat flux [13–17], empirical correlations to predict the partitioning of wall heat flux [14,18,19], and mechanistic correlations for the total heat flux and their partitioning [20–22]. Warrier and Dhir [23] provided a detailed review on these various methods and concluded that mechanistic correlations give a better physical insight into subcooled boiling phenomenon and proposed the use of submodels to define the bubble dynamics. Literature review reveals that boiling in crossflow systems has been extensively studied, but very limited studies have been reported in subcooled boiling regime for these configurations. Huang and Witte [24,25] studied the effect of liquid flow and high subcooling across a bank of horizontal tube bundles and developed a correlation for the heat transfer coefficient using the methodology by Chen [26] developed for saturated nucleate boiling. Shah [27] compared his correlation for heat transfer coefficient around a single-tube, developed for highly subcooled liquid, with various correlations developed for low subcooled liquid and found good agreement. Cornwell [28] studied saturated nucleate flow boiling in tube bundles and attributed the enhancement in heat transfer rates to sliding bubbles. Gupta [29] attributed the enhancement in the heat transfer coefficient during nucleate boiling to the turbulence caused by the presence of bubbles on the surface.

It has been shown that reduction in length scale has a considerable affect on the bubble dynamics and flow characteristics during flow boiling. For subcooled flow boiling this is especially important since the heat transfer mechanism is very dependent on the bubble nucleation process. For example, Lee et al. [30] and Kuo et al. [31] examined the bubble dynamics for water in a microchannel and observed considerable differences compared with conventional scale systems. Cognata et al. [5] performed a visual study on flow pattern in staggered square micro pin fins and observed bubbly, slug, and annular flows. Krishnamurthy and Peles [3] investigated flow boiling heat transfer of water across densely packed staggered micro pin fins—primarily focusing on saturated flow boiling—and found that convective boiling was the dominant heat transfer mechanism.

Based on previous studies, it can be concluded that knowledge about bubble characteristics in diminishing length scales is important to elucidate heat transfer mechanisms. In the current manuscript, flow boiling across a single row of inline micro pin fins entrenched in a microchannel is presented. The microdevice consists of five 200 μm wide and 243 μm deep microchannels, each equipped with an inlet orifice, consisting of 24 columns of 100 μm diameter circular pin fins, with pitch-to-diameter ratio of 4. This study aims to elucidate the local heat transfer coefficient, to identify flow patterns, and to decipher the heat transfer mechanisms. Additionally, the performance of the pin fin device was compared with a plain microchannel device.

2 Device Design

A computer aided design (CAD) schematic of the microdevice, consisting of five 200 μm wide and 243 μm deep microchannels entrenched in a 1800 μm wide channel, is shown in Fig. 1. Each microchannel encompassed 24 inline 100 μm diameter micro pin fins with a pitch-to-diameter ratio of 4. Pressure taps were placed at the inlet and the exit of the microchannel array to enable pressure measurements. A micro-orifice, 400 μm long and 20 μm wide, was fabricated upstream of each microchannel to suppress
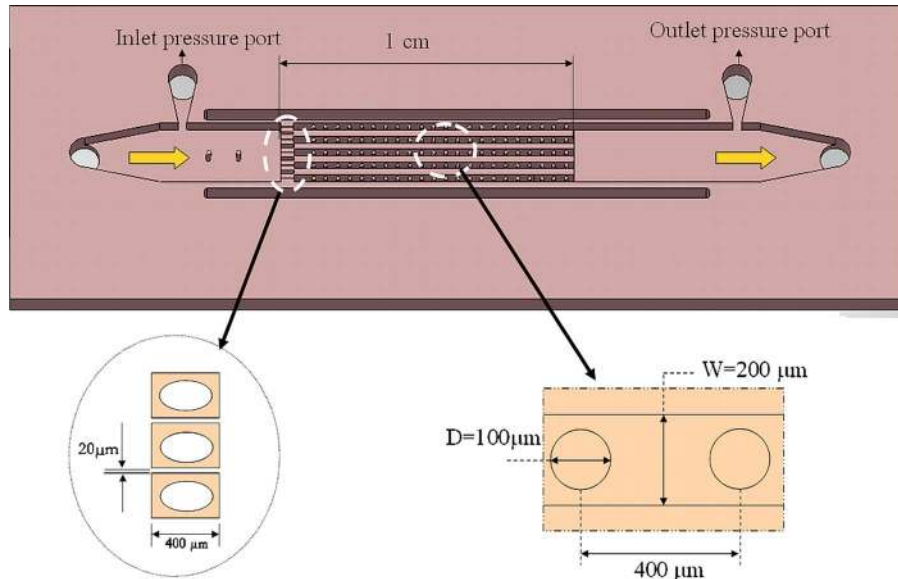
Fig. 1 Device overview showing the device dimensions

flow oscillations. A heater was deposited on the backside of the channel-pin fin section excluding the orifice to provide the requisite heat flux. A thermistor 10 μm wide and 300 μm long was placed 3.33 mm from the channel inlet. A Pyrex cover sealed the device from the top and allowed flow visualization. For details regarding the experimental set up and microfabrication process flow, please refer to Ref. [3].

3 Data Reduction

The voltage and current were used to calculate the input power, while the local temperature from the thermistor was obtained from the calibration curve. Assuming 1D steady state conduction through the silicon block, the local surface temperature of the device was obtained by

$$T_{x,s} = T_{\text{thermistor}} - \frac{(P - Q_{\text{loss}})t_s}{k_s A_p} \tag{1}$$

The local quality was calculated from the known mass flow rate according to

Table 1 Uncertainty of variables

Uncertainty variable	Measurement range	Error
Flow rate, Q [a]	0–18 ml/min	2%
Voltage, V	0–40 V	0.5%
Current, I	0–5 A	0.5%
Ambient temperature, T_{amb}	NA	±1°C
Channel width, w	NA	1%
Channel height, H	NA	0.67%
Density of liquid, ρ_l	NA	0.5%
Mass flux, G	NA	3.4%
Average surface temperature, T_r	NA	±0.5°C
Pressure, p	0–1379 kPa	3.5 kPa
Heat flux, q_w''	NA	3%
Local thermal resistance R_{conv}	NA	12–16%
Local heat transfer coefficient, h_x	NA	12–16%
Average heat transfer coefficient, h	NA	10–15%
Average Nusselt number, Nu	NA	10–15%
Reynolds number, Re_D	NA	3.4%
Boiling number, Bo	NA	11%

[a]The manufacturer provided the flow rate range for water, while experiments were performed with HFE-7000. The flow meter was calibrated prior to experiments.

$$x = \frac{(P - Q_{\text{loss}})(L_x/L_o) - \dot{m}c_p(T_{\text{sat}} - T_i)}{\dot{m}h_{fg}} \tag{2}$$

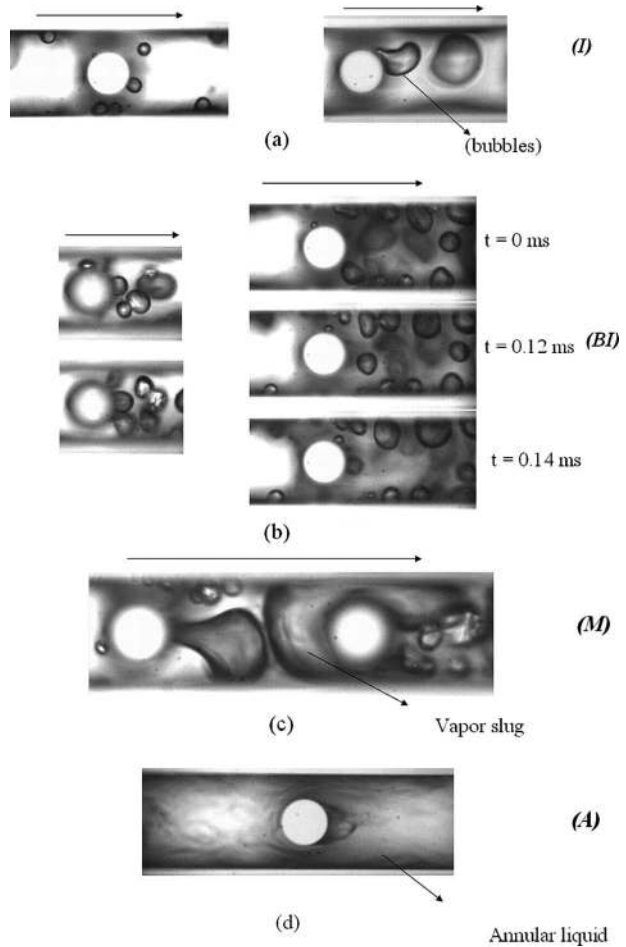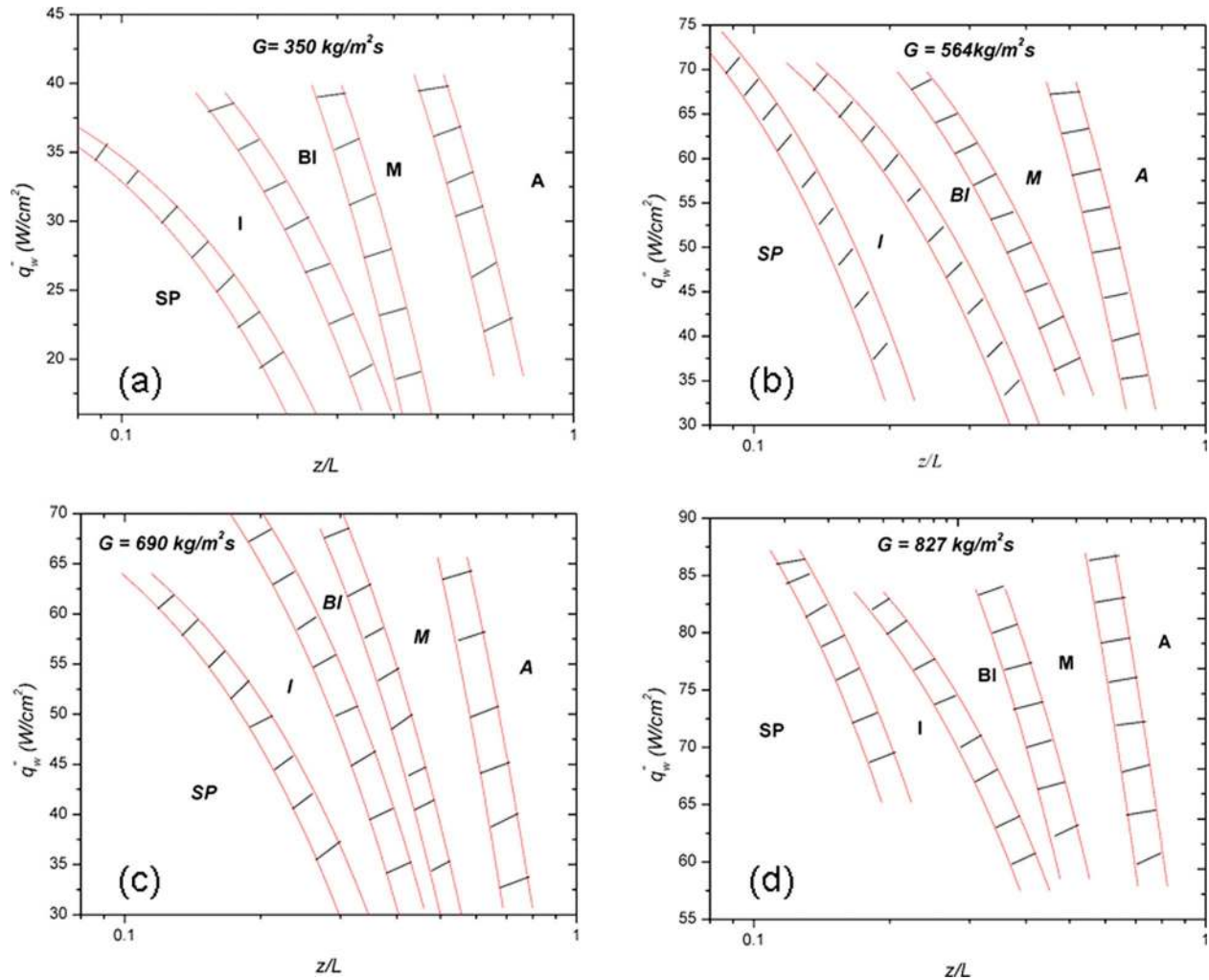The local heat transfer coefficient for the microchannel with pin fins was calculated according to

Fig. 2 Images showing: (*a*) isolated bubble region (*I*), (*b*) bubble interacting (*BI*), (*c*) multiple flow region (*M*), and (*d*) annular flow (*A*)

Fig. 3 Flow maps based on wall heat flux for all the mass fluxes: (*a*) $G=350$ kg/m^2 s, (*b*) $G=564$ kg/m^2 s, (*c*) $G=689$ kg/m^2 s, and (*d*) $G=827$ kg/m^2 s

$$h_x = \frac{P - Q_{\text{loss}}}{A_t(T_{x,s} - T_1)} \tag{3}$$

where $T_1 = T_{mx}$ if $x < 0$ and $T_1 = T_{\text{sat}}$ if $x > 0$. The mean local fluid temperature (T_{mx}) was obtained through an energy balance

$$T_{mx} = T_{mi} + \left(\frac{P - Q_{\text{loss}}}{\dot{m}C_p} \frac{L_x}{L} \right) \tag{4}$$

The total surface area of the channel is given by

$$A_t = N_f \eta_f A_{s,f} + A_b + N_p \eta_p A_{s,p} \tag{5}$$

where

$$\eta_f = \frac{\tanh(m_f H)}{m_f H}, \quad m_f = \sqrt{\frac{h_x(2(W+L))}{k_s WL}},$$

$$\eta_p = \frac{\tanh(m_p H)}{m_p H}, \quad m_f = \sqrt{\frac{h_x(\pi D H)}{k_s \left(\frac{\pi D^2}{4} \right)}}$$

The above equations (Eqs. (3) and (5)) were solved iteratively to obtain the local heat transfer coefficient. Similar methodology was adopted to obtain the heat transfer coefficient for the plain channel, but the total surface area was calculated as

$$A_{t,\text{plain}} = N_f \eta_f A_{s,f} + A_t - N_f A_{s,f} \tag{6}$$

The convective resistance used to evaluate the thermal performance is

$$R_{\text{conv}} = \frac{1}{h_x A_t} \tag{7}$$

The statistical average value of the heat transfer coefficients h_x and the corresponding Nusselt numbers over all heat fluxes for a fixed Reynolds number in the single-phase region was obtained by

$$\bar{h}_x = \frac{1}{M} \sum_{i=1}^{M} h_{x,i} \tag{8}$$

$$\overline{\text{Nu}}_x = \frac{1}{M} \sum_{i=1}^{M} \overline{\text{Nu}}_{x,i} \tag{9}$$

The uncertainties associated with the measured values were obtained from the manufacturers' specification sheets (Table 1) while the uncertainties associated with the derived quantities were obtained by using the propagation of uncertainty analysis, and are also given in Table 1.
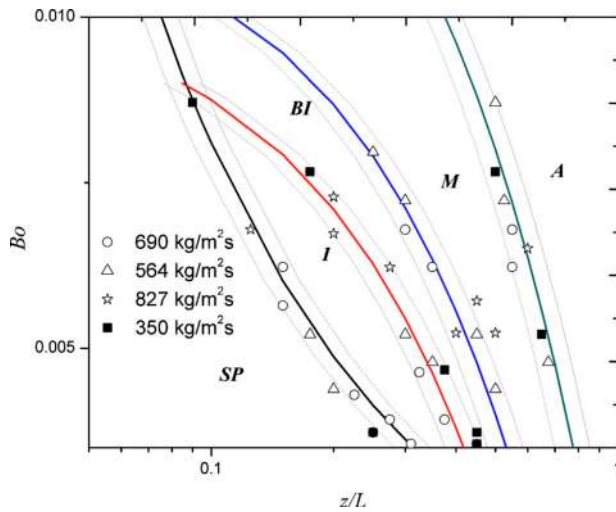
Fig. 4 Flow map showing the different flow patterns along the channel

4 Results and Discussion

4.1 Flow Pattern. In order to determine the dominant flow patterns in the device, images were taken at 10 different locations along the length of the channel. The flow patterns were then manually classified into bubbly flow, multiple flow (M), and annular flow (A). The bubbly flow was further categorized into two regions: isolated bubbles (I) and bubbles interacting (BI). The isolated bubble region extends over a relatively small section of the channel, where bubbles nucleated and departed without coalescing with bubbles from neighboring sites (Fig. 2(a)). With increasing nucleation site density, bubbles began to coalesce (Fig. 2(b)), and formed larger bubbles with diameter smaller than the pin in diameter. Further downstream, these bubbles grew and developed into vapor slugs, which were intermittently sheared by the pin fins and broken into bubbles again. This region where bubbles and vapor slugs coexisted was termed multiple flow (Fig. 2(c)). Eventually, the vapor slugs merged and the flow transitioned to annular flow, where liquid traversed through the channel walls, while vapor propagated through the core—nucleation was suppressed (Fig. 2(d)). In the channel inlet, only liquid single-phase was present. As expected, for a given mass flux, all flow patterns shifted upstream with increasing heat flux. Figures 3(a)–3(d) show a flow maps for all mass fluxes as a function of wall heat flux and normalized axial distance. The hatch regions on the flow map indicate flow transition regions. Visualization measurements were repeated three times to obtain a meaningful statistical average transition zone. In order to obtain a more general flow map using all mass fluxes and heat fluxes, an attempt to collapse the four flow maps into a single map using the boiling number was carried out. This was done by first plotting the above flow maps in terms of the boiling number and normalized axial distance, followed by fitting the data points with a best curve fit, as shown in Fig. 4. 90% of the transition data points fell within ±12% of the transition lines, as shown by the dotted lines in the figure.

4.2 Heat Transfer Coefficient. The local single-phase heat transfer coefficient is shown as a function of the wall heat flux for different mass fluxes in Fig. 5(a). The heat transfer coefficient characteristics followed similar trend to those observed in conventional scale tube bundle systems, i.e., independent of wall heat flux and increasing with mass fluxes. Figure 5(b) also shows the variation in the Nusselt number (Nu$_h$)—defined based on channel hydraulic diameter—as a function of the Reynolds number (Re$_D$). The local heat transfer coefficients during boiling as a function of wall heat flux are shown for different mass fluxes in Figs.
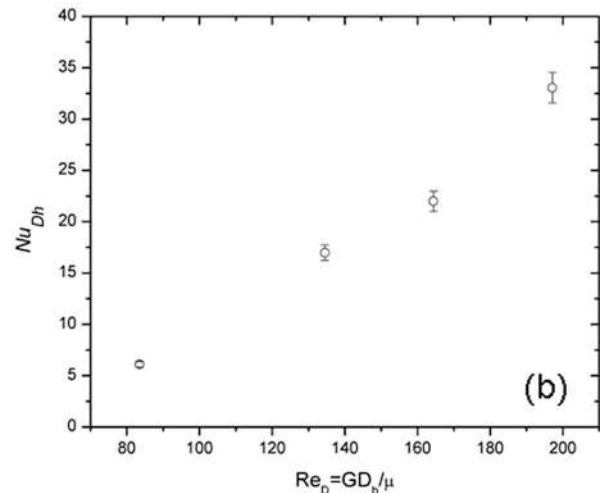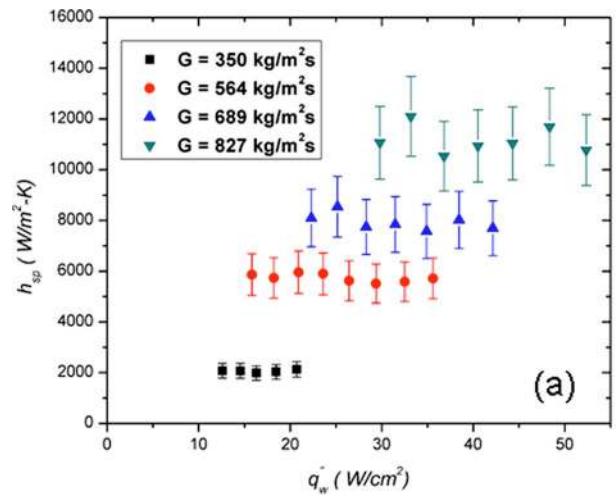

Fig. 5 (*a*) The variation in single-phase heat transfer coefficient as a function of wall heat flux and (*b*) variation in Nusselt number as a function of the Reynolds number

6(a)–6(d) (the exit pressure was maintained at 260 kPa). For G =350 kg/m^2 s, the heat transfer coefficient increased linearly with wall heat flux for $q_w'' < 45$ W/cm^2, and subsequently decreased. Similar decrease in the heat transfer coefficient was also observed for $G=564$ kg/m^2 s at $q_w''=80$ W/cm^2. For mass fluxes of 689 kg/m^2 s and 827 kg/m^2 s, the heat transfer coefficient increased linearly with wall heat flux. Figure 7 shows the variation in the heat transfer coefficient as a function of the local quality for the four mass fluxes. The majority of the datum points corresponding to two-phase flow are in the subcooled boiling regime. Figure 7 also shows that the heat transfer coefficient during subcooled boiling is considerably higher compared with the single-phase heat transfer coefficient. Such an enhancement during heat transfer coefficient in nucleate boiling has been observed in both conventional scale channels and minichannels [32,33] and has been attributed to various mechanisms, such as the evaporation of the microlayer beneath a growing bubble, transient conduction through the cold liquid layer replacing the superheated liquid layer carried away by the departing bubble [21], and sliding bubbles [28]. The contribution of these mechanisms are added linearly to account for the total heat flux according to [21]

$$q_t'' = q_{ev}'' + q_{tr}'' + q_{sp}'' \tag{10}$$

where q_t'', q_{ev}'', q_{tr}'', and q_{sp}'' are the total heat flux, evaporative heat flux, quenching heat flux, and single-phase heat flux, respectively.
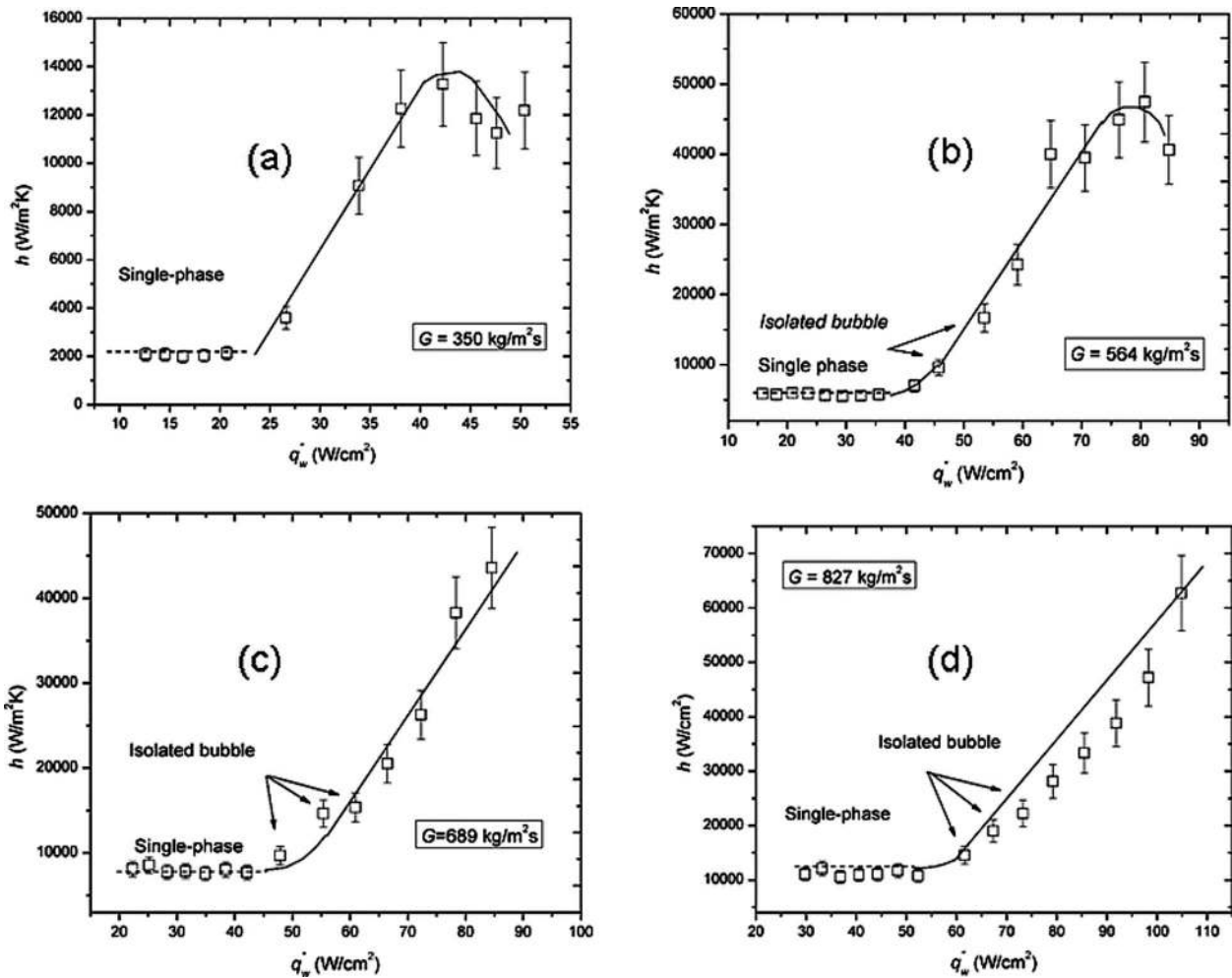
Fig. 6 Heat transfer coefficients as a function of wall heat flux: (*a*) G=350 kg/m^2 s, (*b*) G=564 kg/m^2 s, (*c*) G=689 kg/m^2 s, and (*d*) G=827 kg/m^2 s

The contribution of the above mentioned mechanisms toward the observed enhancement in the heat transfer is assessed below.

5 Heat Transfer Enhancement Mechanisms

Evaporative heat flux. The evaporative heat flux is defined as the latent energy carried away by the bubbles per unit area and

Fig. 7 The variation in heat transfer coefficient as a function of local quality (heat flux in W/cm^2 in parenthesis)

consists of two terms arising from the stationary and sliding bubbles

$$q''_{ev} = q''_{ev,st} + q''_{ev,sl} = fV_d\rho_v N_a h_{fg} + f(V_l - V_d)\rho_v N_a h_{fg} \qquad (11)$$

The stationary bubble heat flux is associated with the growth of the bubble nucleating on the surface, and the sliding bubble is associated with the heat transfer during bubble growth while moving along the surface. In Eq. (11), the bubble departure frequency was assumed to be equal to the bubble lift off frequency—an assumption that is based on observation of many bubbles. Assuming the departing bubble to be spherical, the volume of the departing and lifting bubbles can be calculated as

$$V_d = \frac{\pi D_d^3}{6}, \quad V_l = \frac{\pi D_l^3}{6} \qquad (12)$$

Quenching heat flux. As a bubble departs from a nucleation site, it displaces superheated liquid adjacent to the wall by cold liquid from the bulk flow. Han and Griffith [34] postulated that the departing bubble carries away with it liquid from an area—termed area of influence—that is four times the projected area of the departing bubble. The quenching heat flux was obtained by following the approach adopted by Mikic and Rohsenow [35] assuming pure conduction through the liquid in the area of influence. For any stationary bubble departing from the site, the total average heat flux over the area of influence is given by
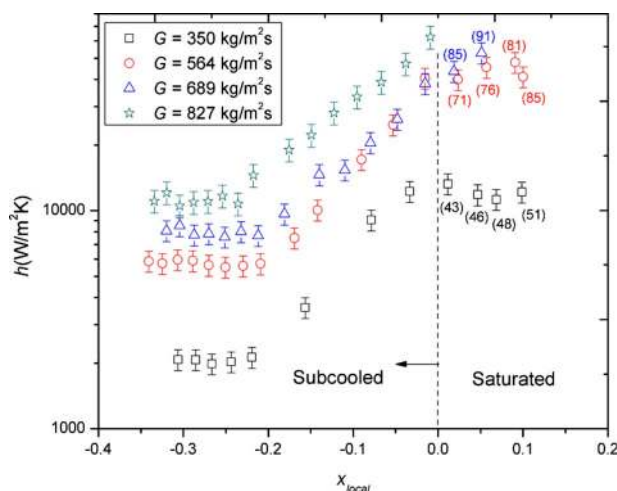
Table 2 Bubble dynamics in the isolated bubble region ($z=2.5-3.5$ mm)

G	q_{ch}	N_{wall}	$N_{\theta=0}$	$N_{\theta=180}$	f_{wall}	$f_{\theta=0}$	$f_{\theta=180}$	$D_{d,wall}$	$D_{d,\theta=180}$	$D_{d,\theta=0}$	q_{ev} (%)	q_{tr} (%)
350	13	2	2	3	3511	413	50	32	18	72	0.62	8.12
350	16.05	5	2	4	4300	1592	445	34	14	55	1.77	7.38
565	19.2	5	2	3	4712	2799	2175	32.5	18.5	74.6	2.6	8.9
565	20.3	10	3	5	3472	3235	2233	40.3	13	70.6	4.8	12.1
689	27.1	16	3	4	2550	4749	481	37.7	10.02	43	2.5	5.2
689	29.9	20	6	4	2819	5095	468	33.6	10.02	30	2.3	5.9
827	36.2	20	4	7	2260	5885	250	41.9	9.22	42	2.8	7.5
827	39.5	25	5	12	3805	6297	110	38	8.9	25	3.96	8.9

$$q''_{tr,st} = 2\sqrt{\pi(k\rho c_p)_l} f D_d^2 N_a (T_w - T_l) \qquad (13)$$

In addition to the stationary bubbles, the bubbles sliding along the surface also displaced the liquid from the surface. Assuming transient conduction through the displaced liquid layer, the total average heat flux over the area swept by the bubble is given by

$$q''_{tr,st} = f \int_0^t \left(\frac{k(T_w - T_l)}{\sqrt{\pi \alpha t}} A_{sl} N_a \right) dt \qquad (14)$$

$$= \frac{2}{\sqrt{\pi}} \sqrt{(k\rho c_p)_l} f A_{sl} N_a (T_w - T_l) \qquad (15)$$

The sliding area for the bubbles was obtained as follows:

$$A_{sl} = D_{av} l = \frac{D_d + D_l}{2} l \qquad (16)$$

l is the sliding distance, which was obtained through flow visualization. The bubble lift off diameter was found to be approximately four times the bubble departure diameter for bubbles nucleating from the frontal stagnation point ($\theta=0$ deg) and twice the bubble departure diameter for bubbles departing from the sidewalls.

It should be noted that the use of Han and Griffith's quenching term might not be entirely adequate to sliding bubbles since a sliding bubble is merely moving the superheat liquid layer along the wall rather than displacing it from the surface. However, it can be argued that because of this the model should overpredict the contribution of a sliding bubble. The analysis about the heat transfer mechanisms discussed in the paper will later show that the contribution of the quenching to the total heat flux is insignificant and therefore, that quenching is not an important heat transfer mechanism in this study. In other words, the use of the quenching model by Han and Griffith [34] serves in this study to demonstrate that it is not an important mechanism rather than to obtain accurate measure of the quenching effect.

The total heat transfer through transient conduction can be added linearly as

$$q''_{tr} = q''_{tr,st} + q''_{tr,sl} \qquad (17)$$

In order to determine the above heat fluxes, the bubble dynamics on the heated wall, such as bubble departure frequency, nucleation site density, and bubble departure diameter are necessary, and were obtained through flow visualization technique discussed in Ref. [36]. Since clear bubble images were required to obtain the parameters defining the bubble dynamics, all images were taken in the isolated bubble region. Figures 6(a)–6(d) also show the conditions under which the isolated bubbles were observed (shown by arrows). Table 2 gives values of various parameters defining the bubble dynamics between $z=2.5$ mm and $z=3.5$ mm. Table 2 also shows the contribution of the evaporative and transient conduction heat fluxes to the total heat flux. Since the bubbles emanated from two angular positions ($\theta=0$ deg, $\theta=180$ deg) [36], the bubble dynamics parameters for these locations were included in the calculation of the evaporative and transient heat fluxes. The

contributions of both the evaporative and the transient conduction heat fluxes toward the total heat flux were insignificant. This shows that another significant mechanism in the form of bulk fluid agitation is a more potent heat transfer mode than the local heat removal (or just the motion) of the superheated layer adjacent to the wall. Basu et al. [21] stated that for regions between the onset of nucleate boiling and onset of significant void—the region where the bubble interaction begin to dominate—the enhancement in the heat transfer coefficient was mainly due to single-phase convection, which was enhanced (by up to 30%) as a result of the presence of bubbles on the surface. The enhancement in the heat transfer coefficient in the current study ranges between 50–90% in the isolated bubble region, which was larger than those observed in conventional scale systems. Based on the values obtained for the evaporative and transient conduction heat fluxes in the current study, it can be concluded that in the isolated bubble region, the observed enhancement in the heat transfer coefficient is neither due to microlayer evaporation nor due to the transient conduction through the liquid layer. It appears that the presence of bubble in the flow has a more pronounced influence on the heat transfer characteristics in the current microscale study than in large scale systems. The relatively large bubble diameter-to-channel hydraulic diameter ratio, compared with conventional scale systems, can significantly alter the flow characteristics in the channel, and thus, the heat transfer mechanisms. For example, the Reynolds number calculated for a bubble of largest diameter (approximately 75 μm) and the highest mean flow velocity in this study (827 kg/m² s) is 124, which corresponds to laminar flow. It can thus be postulated that the bubbles growing on the sidewalls and the pin fins induce wakes downstream the channel (very much similar to the vortex shedding observed in classical fluid dynamics such as flow across cylinders and spheres), which disrupts the boundary layer significantly beyond the region immediately adjacent to the bubble resulting in higher heat transfer coefficient. The small length scale of the channel can significantly amplify the bubble agitation effect. Additionally, the presence of recirculation zone upstream and downstream the pin fin can also contribute significantly toward enhanced mixing, and thus, enhanced heat transfer. Therefore, at low qualities, the observed enhancement can be attributed to bubble agitation and perturbation of the boundary layer. Similar argument was recently made by Donnelly et al. [37] who studied flow across a sliding bubble on an inclined surface and concluded that bubble induced wakes contribute significantly toward heat transfer enhancement. At high qualities, the nucleation site density increased and bubbles began to merge. This in turn increased the evaporation and transient conduction contributions to the total heat flux. At higher qualities (multiple bubble interaction region), the heat transfer enhancement might be due to similar mechanisms observed in a conventional scale.

5.1 Comparison With a Plain Microchannel. To study the effect of the pin fins on the heat transfer coefficient, experiments with plain microchannels were also conducted under similar thermal hydraulic conditions and the thermal resistances of the two devices were compared. The total thermal resistance consists of
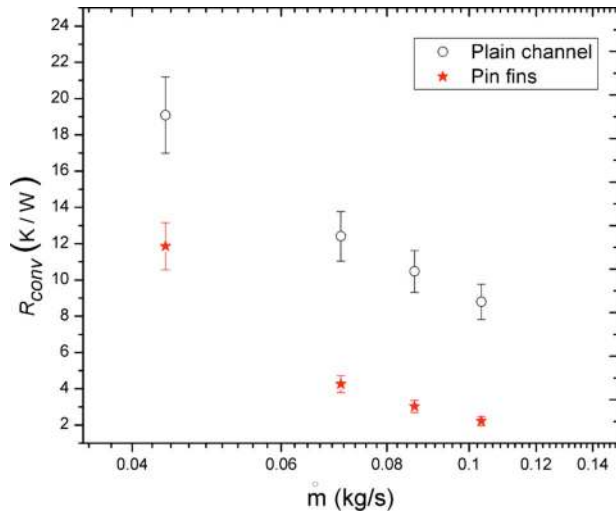
Fig. 8 Comparison of convective resistance as a function of mass flow rate for both devices
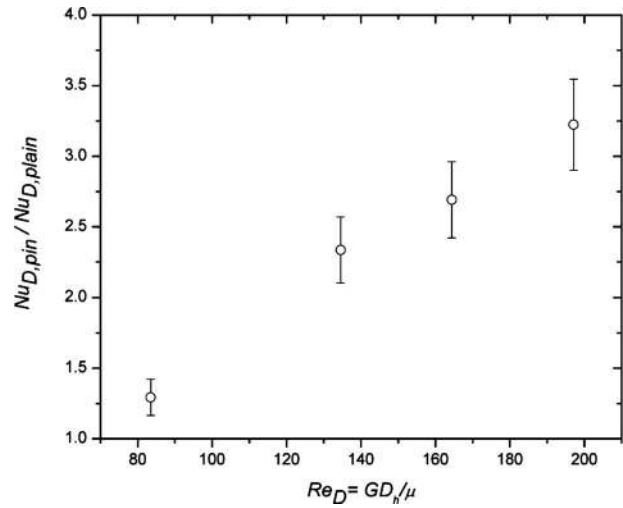

Fig. 9 Enhancement in the single-phase Nusselt number for different Reynolds numbers

conductive resistance (R_{cond}) resulting from heat conduction from the base of the silicon block to the channel surface; sensible heat resistance due to heating of the liquid (R_{heat}); and convective resistance (R_{conv}) resulting from convection from the channel walls

to the fluid. Since the experiments were conducted at similar mass flow rates for both devices, the resistances due to sensible heating were the same. Likewise, the conductive resistance was the same for the two devices. Thus, only the convective resistance was
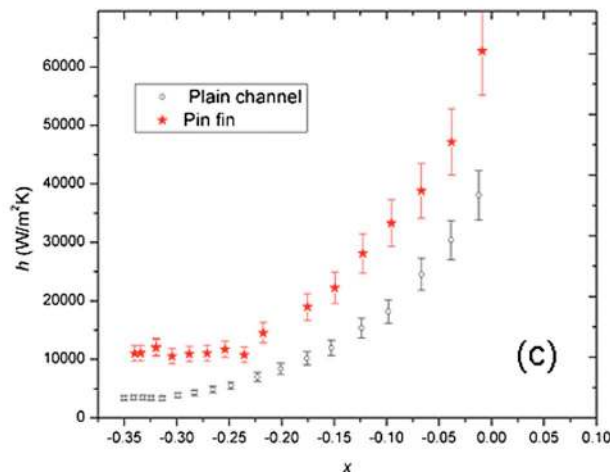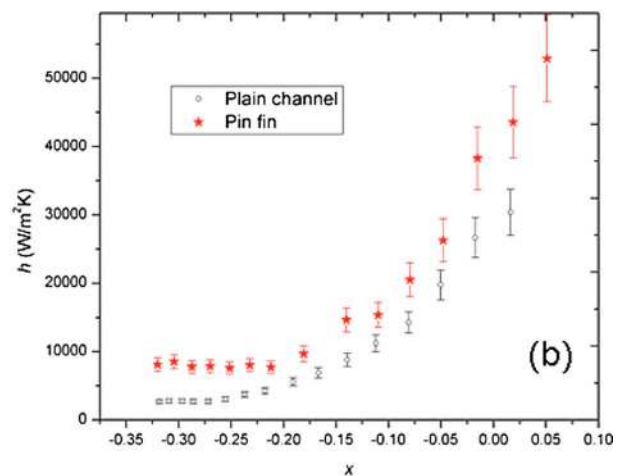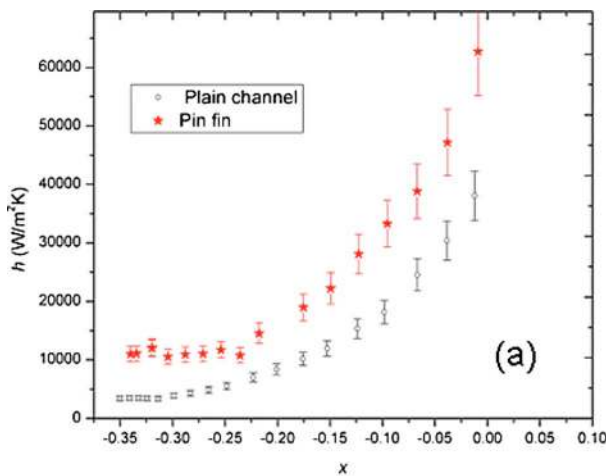

Fig. 10 Comparison of heat transfer coefficients for a microchannel with pin fins and a plain microchannel for different mass fluxes: (a) G_{ch}=282 kg/m² s, (b) G_{ch}=345 kg/m² s, and (c) G_{ch}=413 kg/m² s
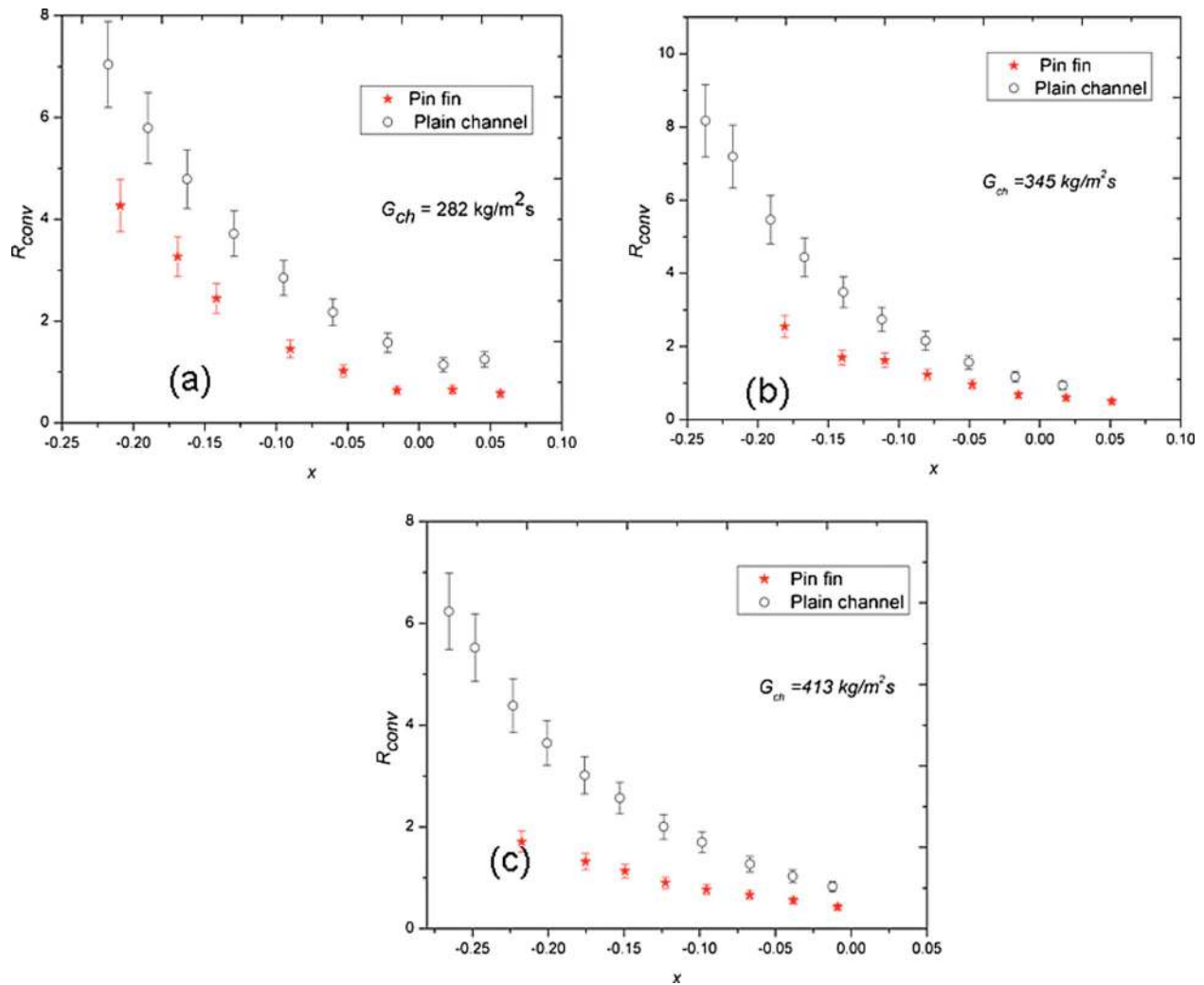
Fig. 11 Comparison of thermal convective resistances for both devices: (*a*) $G_{ch}=282$ kg/m^2 s, (*b*) $G_{ch}=345$ kg/m^2 s, and (*c*) $G_{ch}=413$ kg/m^2 s

evaluated and compared. Figure 8 compares the single-phase convective resistance (Eq. (7)) as a function of mass flow rate for both microchannel systems. The convective resistance decreases with increasing mass flow rate for both devices. The lower thermal resistance of the microchannels with pin fins compared with the plain microchannel is a result of the higher heat transfer coefficient and larger surface area. Figure 9 compares the ratio of the Nusselt number—based on the channel hydraulic diameter—for both devices as a function of Reynolds number (Re_D defined based on hydraulic diameter of the channel). The enhancement of the heat transfer coefficient increased from 1.3 to 3 when the Reynolds number increased from 84 to 197. Therefore, in addition to the surface area enhancement ($A_{pin}=1.25 \ A_{plain}$), the presence of pin fins significantly affects the hydrodynamic characteristics of the flow resulting in increased heat transfer coefficient. The enhancement increase with the Reynolds number can be attributed to the wake interaction between the pin fins. At low Reynolds number, the wake interaction is less rigorous, and thus, a lower enhancement in the heat transfer coefficient was observed. But at higher Reynolds number, the interaction between the wakes increased, promoting advection (mixing), and thus, reducing the thermal resistance. Figures 10(*a*)–10(*c*) show the heat transfer coefficient as a function of mass quality for both devices. The heat transfer coefficient followed similar trend with respect to quality, but was quantitatively lower for the plain microchannel for all mass fluxes. The comparison of the convective resistance as a

function of local quality (Figs. 11(*a*)–11(*c*)) also shows that the resistance is lower for the microchannel with pin fins. It is also evident that the rate at which the convective resistance decreases for the plain microchannel is higher compared with that observed in the microchannel with pin fins. This can partly be attributed to the more rapid decrease in the fin efficiency of the micro pin fins compared with that of channel sidewalls. Thus, with increasing heat flux, the effective surface area of the microchannel with pin fins decreased more rapidly compared with that of plain microchannel. As a result, the resistance of the microchannel with pin fins decreases more moderately. Nevertheless, the heat transfer is still enhanced by convective mixing of the pin fins, which lowers the convective resistances compared with plain microchannel. The enhancement in heat transfer coefficient is quantified by an enhancement factor E_p defined as

$$E_p = \frac{h_{pin \ fin}}{h_{plain}} \qquad (18)$$

Figure 12 shows the variation in the enhancement factor for different qualities. The enhancement in the two-phase heat transfer coefficient is smaller when compared with the enhancement observed during single-phase. As discussed previously, the enhancement in the two-phase heat transfer coefficient in the isolated bubble region is due to bubble agitation and the perturbation of the boundary layer by the bubbles. Unlike in channel with micro-
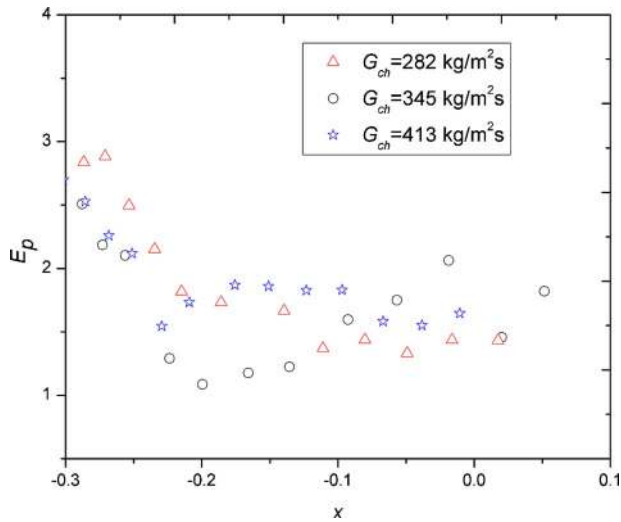
Fig. 12 Enhancement in the heat transfer coefficient for a microchannel with pin fins as a function of mass quality

pin fins, where the presence of pin fins shadows the agitation affect, in plain microchannel, such agitation can affect extended regions of the channel. As a result, the heat transfer coefficient for the plain channel increases at a higher rate compared with microchannel with pin fins in the isolated bubble region. But with increasing heat flux, for the microchannel with pin fins in the multiple bubble interaction region, the heat transfer coefficient increases significantly due to convective mixing aided by the presence of the pin fins. It follows that the enhancement increases after reaching a minimum, which was observed for both G_{ch} =282 kg/m^2 s and G_{ch}=417 kg/m^2 s.

6 Summary

Subcooled and low quality saturated flow boiling across micro pin fins entrenched in a microchannel was studied for various mass fluxes and heat fluxes. The following summarizes the main findings of this study.

- Flow visualization revealed the existence of isolated bubbles, bubbles interacting, multiple flow pattern, and annular regions along the channel length. The observed flow patterns were mapped as a function of the boiling number along the channel length.
- Single-phase heat transfer coefficient for the microchannels with pin fins was found to be considerably higher compared with the plain wall channels. This was attributed to a combination of enhanced area and mixing.
- Considerable enhancement in the heat transfer coefficient during subcooled boiling over the corresponding single-phase heat transfer coefficient was observed. In the isolated bubbles region, this enhancement was attributed to the agitation of the liquid due to bubble protrusion and disruption of the boundary layer.
- The heat transfer coefficient during subcooled boiling for the microchannel with pin fins was higher than the corresponding value for plain microchannel. But the enhancement in the heat transfer coefficient was smaller in comparison to that observed during single-phase flow, especially in the isolated bubble region. This was attributed to the reduction in fin efficiency.

Acknowledgment

Nomenclature

$$A_p = \text{platform area (m}^2)$$
$$A_t = \text{total surface area (m}^2)$$
$$A_{sl} = \text{sliding area swept by bubbles (m}^2)$$
$$\text{Bo} = \text{boiling number } (q''_{ch}/Gh_{fg})$$
$$c_p = \text{specific heat capacity (kJ/kg K)}$$
$$D = \text{diameter of pin fin (m)}$$
$$D_h = \text{hydraulic channel diameter (m)}$$
$$D_d = \text{bubble departure diameter (m)}$$
$$D_l = \text{bubble lift off departure diameter (m)}$$
$$E_p = \text{enhancement factor}$$
$$f = \text{bubble departure frequency (Hz)}$$
$$G = \text{mass flux (kg/m}^2 \text{ s)}$$
$$h_{fg} = \text{latent heat of vaporization (kJ/kg)}$$
$$h_x = \text{local heat transfer coefficient (W/m}^2 \text{ K)}$$
$$H = \text{height of microchannel (m)}$$
$$I = \text{current (A)}$$
$$k_s = \text{substrate thermal conductivity (W/m K)}$$
$$L = \text{length of the channel (m)}$$
$$\dot{m} = \text{mass flow rate (kg/s)}$$
$$N_a = \text{nucleation site density}$$
$$N_f = \text{number of fins}$$
$$N_p = \text{number of pin fins}$$
$$\text{Nu}_x = \text{local Nusselt number based on characteristic}$$
$$\text{length scale } (hD/k_f; hD_h/k_f)$$
$$P = \text{power (W)}$$
$$q''_{ev} = \text{evaporative heat flux (W/m}^2)$$
$$q''_{ev,st} = \text{stationary bubble evaporative heat flux}$$
$$\text{(W/m}^2)$$
$$q''_{ev,sl} = \text{sliding bubble evaporative heat flux (W/m}^2)$$
$$q''_{tr,st} = \text{stationary bubble quenching heat flux (W/m}^2)$$
$$q''_{tr,sl} = \text{sliding bubble quenching heat flux (W/m}^2)$$
$$Q_{loss} = \text{heat loss (W)}$$
$$\text{Re}_D = \text{Reynolds number based on channel hydraulic}$$
$$\text{diameter } (GD_h/\mu)$$
$$R_{conv} = \text{thermal convective resistance (K/W)}$$
$$R_{cond} = \text{thermal conductive resistance (K/W)}$$
$$R_{heat} = \text{resistance due to sensible heating of fluid}$$
$$\text{(K/W)}$$
$$T_l = \text{liquid temperature (K)}$$
$$T_{mx} = \text{local fluid temperature (K)}$$
$$T_{mi} = \text{inlet fluid temperature (K)}$$
$$T_{sat} = \text{saturation temperature (K)}$$
$$T_{x,s} = \text{local surface temperature (K)}$$
$$T_{thermistor} = \text{temperature of thermistor (K)}$$
$$t_s = \text{substrate thickness (m)}$$
$$V = \text{voltage (V)}$$
$$W = \text{width of rectangular pin fin (m)}$$
$$x = \text{vapor quality}$$

Symbol

$$\eta_f = \text{fin efficiency}$$
$$\eta_p = \text{pin fin efficiency}$$
$$\rho_v = \text{vapor density}$$
$$\theta = \text{radial angle}$$

References

[1] Qu, W., and Siu-Ho, A., 2008, "Liquid Single-Phase in an Array of Micro-Pin-Fin—Part I: Heat Transfer Characteristics," ASME J. Heat Transfer, **130**(12),

p. 122402.

[2] Qu, W., and Siu-Ho, A., 2008, "Liquid Single-Phase in an Array of Micro-Pin-Fin—Part II: Pressure Drop Characteristics," ASME J. Heat Transfer, **130**(12), p. 124501.

[3] Krishnamurthy, S., and Peles, Y., 2008, "Flow Boiling of Water in a Circular Staggered Micro-Pin Fin Heat Sink," Int. J. Heat Mass Transfer, **51**(5–6), pp. 1349–1364.

[4] Siu-Ho, A., Qu, W., and Pfefferkorn, F., 2007, "Experimental Study of Pressure Drop and Heat Transfer in a Single-Phase Micropin-Fin Heat Sink," ASME J. Electron. Packag., **129**(4), pp. 479–487.

[5] Cognata, T. J., Hollingsworth, K. D., and Witte, L. C., 2007, "High-Speed Visualization of Two-Phase Flow in a Micro-Scale Pin-Fin Heat Exchanger," Heat Transfer Eng., **28**(10), pp. 861–869.

[6] Prasher, R. S., Dirner, J., Chang, J.-Y., Myers, A., Chau, D., He, D., and Prstic, S., 2007, "Nusselt Number and Friction Factor of Staggered Arrays of Low Aspect Ratio Micropin-Fins Under Cross Flow for Water as Fluid," ASME J. Heat Transfer, **129**(2), pp. 141–153.

[7] Koşar, A., and Peles, Y., 2006, "Convective Flow of Refrigerant (R-123) Across a Bank of Micro Pin Fins," Int. J. Heat Mass Transfer, **49**, pp. 3142–3155.

[8] Krishnamurthy, S., and Peles, Y., 2007, "Gas-Liquid Two-Phase Flow Across a Bank of Micro Pillars," Phys. Fluids, **19**(4), p. 043302.

[9] Koşar, A., and Peles, Y., 2007, "Boiling Heat Transfer in a Hydrofoil-Based Micro Pin Fin Heat Sink," Int. J. Heat Mass Transfer, **50**(5–6), pp. 1018–1034.

[10] Koşar, A., and Peles, Y., 2007, "Micro Scale Pin Fin Heat Sinks Parametric Performance Evaluation Study," IEEE Trans. Compon. Packag. Technol., **30**(4), pp. 855–865.

[11] Siu-Ho, A. M., Qu, W., and Pfefferkorn, F. E., 2006, "Pressure Drop and Heat Transfer in a Single-Phase Micro-Pin-Fin Heat Sink," ASME Paper No. IMECE2006 14777.

[12] Krishnamurthy, S., and Peles, Y., 2008, "Two-Phase Flow Pattern Transition Across Micropillars Size Scale Effect at the Micro Scale," Phys. Fluids, **2**, p. 023602.

[13] Bjorg, R. W., Hall, G. R., and Rohsenow, W. M., 1982, "Correlation of Forced Convection Boiling Heat Transfer Data," Int. J. Heat Mass Transfer, **25**, pp. 753–757.

[14] Bowring, R. W., 1962, "Physical Model Based on Bubble Detachment and Calculation of Steam Voidage in the Subcooled Region of a Heated Channel," Institutt for Atomenergi, Halden, Norway, Paper No. Hpr-10.

[15] Bergles, A. E., and Rohsenow, W. M., 1964, "The Determination of Forced Convection, Surface Boiling Heat Transfer," ASME J. Heat Transfer, **86**, pp. 365–372.

[16] Kutateladze, S. S., 1961, "Boiling Heat Transfer," Int. J. Heat Mass Transfer, **4**, pp. 31–45.

[17] Kandlikar, S. G., 1998, "Heat Transfer and Flow Characteristics in Partial Boiling, Fully Developed Boiling, and Significant Void Flow Regions of Subcooled Flow Boiling," ASME J. Heat Transfer, **120**, pp. 395–401.

[18] Rouhani, S. Z., and Axelsson, E., 1970, "Calculation of Void Volume Fraction in the Subcooled and Quality Boiling Regions," Int. J. Heat Mass Transfer, **13**, pp. 383–393.

[19] Lahey, R. T., 1978, "A Mechanistic Subcooled Boiling Model," *Proceedings of the Sixth International Heat Transfer Conference*, Vol. 1, Toronto, Canada, pp. 292–297.

[20] Del Valle, V. H. M., and Kenning, D. B. R., 1985, "Subcooled Flow Boiling at High Heat Flux," Int. J. Heat Mass Transfer, **28**, pp. 1907–1920.

[21] Basu, N., Warrier, G. R., and Dhir, V. K., 2005, "Wall Heat Flux Partitioning During Subcooled Flow Boiling—Part I: Model Development," ASME J. Heat Transfer, **127**, pp. 131–140.

[22] Basu, N., Warrier, G. R., and Dhir, V. K., 2005, "Wall Heat Flux Partitioning During Subcooled Flow Boiling—Part II: Model Validation," ASME J. Heat Transfer, **127**, pp. 141–148.

[23] Warrier, G. R., and Dhir, V. K., 2006, "Heat Transfer and Wall Heat Flux Partitioning During Subcooled Flow Nucleate Boiling, A Review," ASME J. Heat Transfer, **128**, pp. 1243–1256.

[24] Huang, L.-D., and Witte, L., 2001, "Highly Subcooled Boiling in Crossflow," ASME J. Heat Transfer, **123**, pp. 1080–1085.

[25] Huang, H. L., and Witte, L. C., 1996, "An Experimental Investigation of the Effects of Subcooling and Velocity on Boiling of Freon-113," ASME J. Heat Transfer, **118**, pp. 436–441.

[26] Chen, J. C., 1966, "Correlation for Boiling Heat Transfer to Saturated Fluids in Convective Flow," I&EC Process Des. Dev., **5**(3), pp. 322–329.

[27] Shah, M. M., 2005, "Improved General Correlation for Subcooled Boiling Heat Transfer During Flow Across Tubes and Tube Bundles," HVAC&R Res., **11**(2), pp. 285–303.

[28] Cornwell, K., 1990, "The Influence of Bubbly Flow on Boiling From a Tube in a Bundle," Int. J. Heat Mass Transfer, **33**(12), pp. 2579–2584.

[29] Gupta, A., 2005, "Enhancement of Boiling Heat Transfer in a 5×3 Tube Bundle," Int. J. Heat Mass Transfer, **48**, pp. 3763–3772.

[30] Lee, P. C., Tseng, F. G., and Pan, C., 2004, "Bubble Dynamics in Micro Channels. Part I: Single Microchannel," Int. J. Heat Mass Transfer, **47**, pp. 5575–5589.

[31] Kuo, C.-J., Koşar, A., Peles, Y., Virost, S., Mishra, C., and Jensen, M., 2006, "Bubble Dynamics During Boiling in Enhanced Surface Microchannels," J. Microelectromech. Syst., **15**(6), pp. 1514–1527.

[32] Lie, Y., and Lin, T., 2006, "Subcooled Flow Boiling Heat Transfer and Associated Bubble Characteristics of R-134a in a Narrow Annular Duct," Int. J. Heat Mass Transfer, **49**, pp. 2077–2089.

[33] Martín-Callizo, C., Palm, B., and Owhaib, W., 2007, "Subcooled Flow Boiling of R-134a in Vertical Channels of Small Diameter," Int. J. Multiphase Flow, **33**, pp. 822–832.

[34] Han, C., and Griffith, P., 1965, "The Mechanism of Heat Transfer in Nucleate Pool Boiling, Bubble Initiation, Growth and Departure," Int. J. Heat Mass Transfer, **8**, p. 887904.

[35] Mikic, B. B., and Rohsenow, W. M., 1969, "A New Correlation of Pool-Boiling Data Including the Effect of Heating Surface Characteristics," ASME J. Heat Transfer, **44**(14), pp. 245–250.

[36] Krishnamurthy, S., and Peles, Y., 2010, "Flow Boiling on Micropin Fins Entrenched Inside a Microchannel—Flow Patterns and Bubble Departure Diameter and Bubble Frequency," ASME J. Heat Transfer, **132**(4), p. 041002.

[37] Donnelly, B., O'Donovan, T. S., and Murray, D. B., 2009, "Surface Heat Transfer Due to Sliding Bubble Motion," Appl. Therm. Eng., **29**(7), pp. 1319–1326.